Band structure of polycrystalline Sb$_4$Mo$_{20}$O$_{62}$ compounds

A. Bonnet, A. Conan, and H. Queinnec

Laboratoire de Physique des Matériaux et Composants de l'Electronique Institut de Physique, Université de Nantes,
F-44072 Nantes, France

M. Ganne and M. Dion

Laboratoire de Chimie Minérale A, Institut de Chimie, Université de Nantes, F-44072 Nantes, France

Transport-coefficient measurements (electrical conductivity, thermoelectric power, and Hall coefficients have been performed on a compact Sb$_4$Mo$_{20}$O$_{62}$ polycrystalline compound in a wide temperature range (130—500 K). Experimental results are interpreted with the help of a p-type semiconductor model with two inverted deep levels near the mid-gap. Conduction mechanisms are governed by acoustical-phonon scattering of the carriers. EPR measurements confirm the theoretical model, which has been retained. Lastly, the model is discussed on the basis of an idealized projection of the Sb$_4$Mo$_{20}$O$_{62}$ structure. The top of the valence band is assumed to be formed from the d_{xy} orbitals of some Mo atoms leading to narrow bonding π bands while the donor and acceptor levels may be formed from the nonbonding d_{xy} orbitals of some Mo atoms of the distorted octahedron framework.

I. INTRODUCTION

The electronic and structural properties of transition-metal oxides have received much recent attention, and among them, in particular, the tungsten trioxide has been studied for its photochromic and electrochromic properties. Many tungsten bronzes, which are nonstoichiometric compounds of the general formula M_xWO$_3$, where M is one of a number of metal cations, have been described by Goodenough.[1] These materials crystallize in several different symmetries depending upon the size and valence of the ion M and its concentration x. The majority of the studies of the tungsten bronzes have centered on the cubic phase. Of the elements for which this phase is possible, Na$_x$WO$_3$ shows a metal-nonmetal transition for a weak concentration of the inserted element due to the fact that the tungsten is not fully oxidized, which may cause an electronic contribution to the conductivity.

Molybdenum phases M_xMoO$_{3+y}$ where M is a monovalent (K,Na) or a divalent (Ba,Sr,Ca) cation[2] have also been studied in extensive detail. More recently, molybdenum bronzes with a trivalent cation have been synthetized by Parmentier et al.[3] They have studied two new phases: Sb$_4$Mo$_{20}$O$_{62}$ and Sb$_8$Mo$_{20}$O$_{62}$. The crystal structure of Sb$_4$Mo$_{20}$O$_{62}$ is described in a framework of corner-sharing MoO$_6$ octahedra (Fig. 1). The symmetry of the phase is orthorhombic [intergrowth tungsten bronze (ITB)]. The pseudohexagonal channels are fully occupied with Sb$_2$O chains. Two covalent bondings are "formed" between the Sb atom and two oxygen atoms of the framework MoO$_3$, and a third one between Sb and the oxygen in the hexagonal channel. To our knowledge, no band-structure model has been determined for transition-metal bronzes with M—O—M chains.

dc electrical conductivity (σ), thermoelectric power (S), and Hall coefficient (R_H) measurements have been performed on compact Sb$_4$Mo$_{20}$O$_{62}$ polycrystalline compounds in the temperature range 130 — 500 K. The experimental results show a p-type semiconducting behavior. In order to explain the transport measurements, a model of a semiconductor with two inverted deep levels which pins the Fermi level near the middle of the forbidden gap has been used. Conduction mechanisms are governed by acoustical-phonon scattering of the carriers. EPR measurements, performed between 80 and 300 K on the same samples, confirm the theoretical values which have been deduced from the transport measurements.
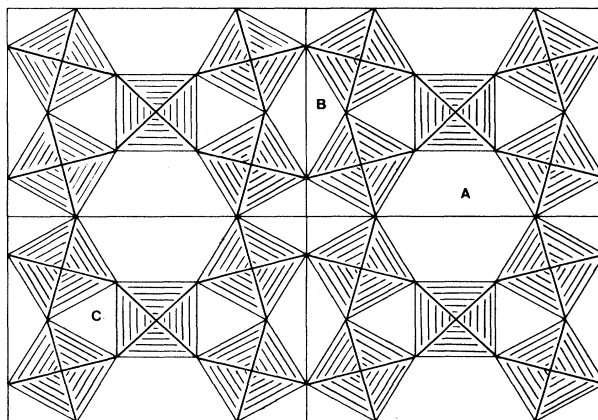
FIG. 1. Molybdenum-oxygen skeleton of the ITB structure. The different types of cavities (A, B, and C) are shown.

II. EXPERIMENTAL PROCEDURE

A. Preparation

The starting materials used are the oxides Sb_2O_3, MoO_3, and metallic Mo weighed in appropriate proportions according to the following reaction:

$$2Sb_2O_3 + \tfrac{56}{3}MoO_3 + \tfrac{4}{3}Mo \rightarrow Sb_4Mo_{20}O_{62} ,$$
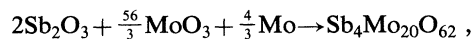
and thoroughly mixed in an agate mortar. The mixture is sealed in an evacuate silica ampoule and heated at 350 °C for one day and at 540 °C for three days. After the heat treatment, no particular precaution is taken to quench them especially rapidly. X-ray diffraction analysis has shown that the lattice parameters are in general agreement with reported values (Table I).

For electrical measurements, the resulting powder is pressed in $3 \times 3 \times 15$ mm^3 bars yielding samples having 80% of the theoretical density. The sample is bound on a thin mica sheet with a highly-electrical-resistive and thermal-conductive epoxy resin. The solders of two copper-constantan thermocouples are inserted in small wells ($\phi = 0.2$ mm) bored at each end of the sample and held with conducting gold paint. Each thermocouple is reeled into a flat coil and bound to the regulated copper holder with the epoxy resin, close to the end of the sample. This procedure minimizes the thermal losses.

Thermoelectric power (TEP) measurements are preformed using a method described previously.[4] The sample is placed between two microheaters made with constantan wire wrapped round an aluminium oxide tubing ($\phi = 1$ mm). The thermal emf's between the two copper and the two constantan wires are measured simultaneously by two digital nanovoltmeters. The help of a data acquisition system monitored by a calculator is required. All the numerical values are calculator controlled.

For electrical resistance measurements, the two constantan wires act as current leads while the potential difference is measured between the two copper wires. The error arising from thermal emf's is canceled by inverting the current. In order to have access to the electrical conductivity, a room-temperature conductivity measurement is performed using the Van der Pauw method.

A double ac method has been used for measuring the Hall voltage in the temperature range 140—310 K. A single-pilot oscillator produces the electric current and the magnetic field. The sample is placed in an electromagnet which is arranged inside a cryostat under vacuum.[5] Complementary dc Hall-coefficient measurements have been performed in order to extend the temperature range up to 450 K. All the high-temperature measurements were performed in an inert gas (He) at a pressure of 10^{-1} bars.

TABLE I. Lattice parameters in general agreement with reported values as shown by x-ray diffraction analysis.

$Sb_4Mo_{20}O_{62}$	a (Å)	b (Å)	c (Å)
From Parmentier *et al.* (Ref. 3)	20.23	8.09	7.17
Our results	20.031	8.098	7.197
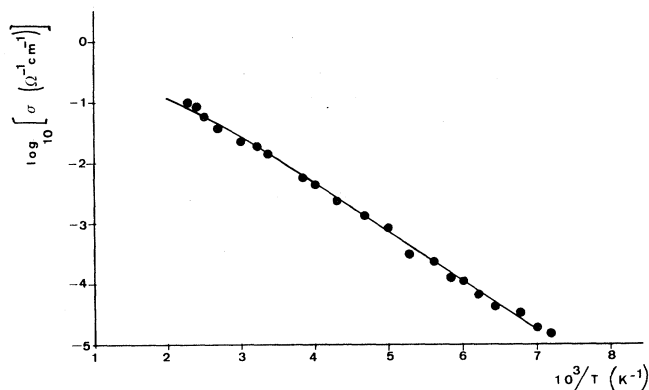
FIG. 2. Experimental variations of $\log_{10}\sigma$ versus $10^3/T$ obtained on $Sb_4Mo_{20}O_{62}$. The theoretical variations are drawn in the solid line.

B. Experimental results

Measured values of the conductivity σ of $Sb_4Mo_{20}O_{62}$ over the temperature range 130—500 K are given in Fig. 2. The results are plotted as $\log_{10}\sigma$ versus $10^3/T$. The conductivity varies quasilinearly from 10^{-5} $\Omega^{-1}cm^{-1}$ at 130 K to 0.13 $\Omega^{-1}cm^{-1}$ at 500 K. Thus the electrical conductivity may be given by $\sigma = \sigma_0 \exp - Ea/2kT$. The room-temperature conductivity is found equal to 0.018 $\Omega^{-1}cm^{-1}$. These mean values are deduced from measurements performed on many samples being issued from different preparations: At most, 5% variations have been observed between the different samples. The thermal activation energy E_a is nearly equal to 0.32 eV for all the samples.

The preexponential factor σ_0 variations can be explained by the different compactnesses of the pressed bars. The TEP variations as a function of the reciprocal temperature are plotted in Fig. 3 in the temperature range 130—500 K. The TEP which is positive, is a decreasing function of the temperature. The TEP variations are quasilinear between 140 and 310 K. Beyond this temperature, the slope of the curve becomes higher and the TEP
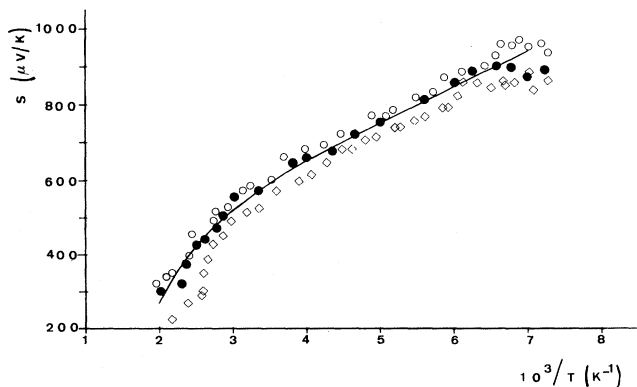
FIG. 3. Experimental variations of the TEP S versus $10^3/T$ obtained on $Sb_4Mo_{20}O_{62}$. The theoretical variations are drawn in the solid line.
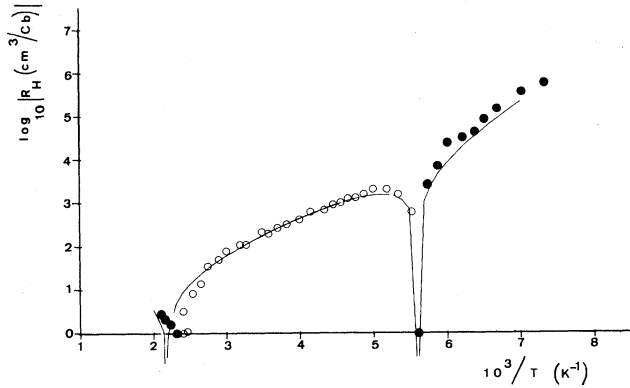
FIG. 4. Experimental variations of $\log_{10}|R_H|$ versus $10^3/T$ obtained on $Sb_4Mo_{20}O_{62}$. ●, R_H is negative; ○, R_H is positive. The theoretical variations are drawn in the solid line.

decreases to the value 350 μV/K at 500 K. The TEP variations (20%) observed between the different samples are greater than those which are observed in electrical conductivity measurements.

The $\log|R_H|$ variations as a function of $10^3/T$ are given in Fig. 4. R_H varies from about -0.3 m^3 at 130 K to a positive maximum ($\simeq +1.4 \times 10^{-3}$ m^3/C) at 190 K, with the Hall coefficient canceling at about 175 K. For higher temperatures, R_H decreases regularly, canceling again at about 410 K. The quasilinear decrease of $\log_{10}|R_H|$ from 190 to 270 K (R_H being positive) is due to the fact that the p/n ratio is nearly constant in this temperature range: The thermal activation energy is 0.17 eV to be compared to the value deduced from electrical conductivity measurements (0.16 eV) (Fig. 5). All these experimental results i.e., the thermally activated conductivity and Hall coefficient and high TEP value (900 μV/K at 140 K), show a p-type semiconducting behavior.

III. DISCUSSION

The quasilinear $\log_{10}\sigma$ variations versus $10^3/T$, compared to the characteristic T dependence of the Hall coef-
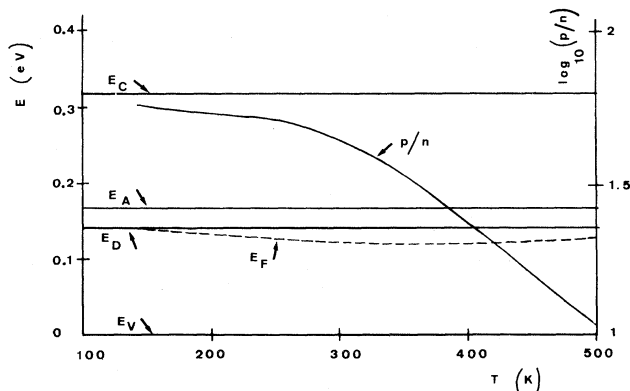
FIG. 5. Theoretical variations of the Fermi-level position versus T are drawn in the dashed line. Theoretical variations of $\log_{10}(p/n)$ versus T are drawn in the solid line.

ficient which cancels twice, suggests the hypothesis of a pinned Fermi level. Therefore, a model of a semiconductor with two inverted deep levels E_A and E_D which effectively pins the Fermi level near the midgap has been tested.

The equation of electrical neutrality is $p + N_D^+ = n + N_A^-$ where p, n, N_D^+, and N_a^-, are, respectively, the densities of electrons, holes, and ionized donor and acceptor levels. By setting $\exp[-\beta(E_F - E_i)] = X$, it can be written that

$$n = \frac{N_c}{X}\exp\left[-\beta\frac{\Delta}{2}\right], \quad p = N_v X \exp\left[-\beta\frac{\Delta}{2}\right]$$

with

$$N_c = \frac{1}{4}\left[\frac{2m_c kT}{\pi h^2}\right]^{3/2}$$

and

$$N_v = \frac{1}{4}\left[\frac{2m_v kT}{\pi h^2}\right]^{3/2},$$

and m_c and m_v are the density of states of electrons and holes, respectively.[6,7] Following Refs. 6 and 8, the densities of ionized donor and acceptor levels are given by

$$N_A^- = \frac{N_A}{1 + 2X\exp[\beta(E_A - E_i)]},$$

$$N_D^+ = \frac{N_D}{1 + (2/X)\exp[-\beta(E_D - E_i)]},$$

where $\Delta = E_c - E_V$ is the forbidden gap and E_i is the midgap energy.

It is a fourth-degree equation in X which has been solved by iteration. In order to save the computation time, only some typical experimental values agreeing with $\log_{10}\sigma$, S, and R_H have been retained.

In our model, the assumption of a T-independent energy gap has been made. Electrons and holes are assumed to be only scattered by acoustical-lattice vibrations. For this type of scattering, the mobility varies as T^{α_n} with $\alpha_n = -\frac{3}{2}$.[6,7]

In the two-band model, the resultant electrical conductivity is obtained by adding the electrical conductivities of each group supposed to be acting independently. So, for all of the temperature range investigated, σ, is given by

$$\sigma = \sigma_n + \sigma_p$$

with

$$\sigma_n = ne\mu_n = ne\mu_n^0\left[\frac{T}{T_0}\right]^{\alpha_n}$$

and

$$\sigma_p = pe\mu_p = \pi\mu_p^0\left[\frac{T}{T_0}\right]^{\alpha_p},$$

where T_0 is the room temperature and μ_n^0 and μ_p^0 are the room-temperature mobilities.

The resultant TEP is a balance between the contribu-

TABLE II. Values of physical constants obtained on compact $Sb_4Mo_{20}O_{62}$ polycrystalline compounds. Theoretical values are enclosed in parentheses.

Δ (meV)	N_v (cm^{-3})	N_c (cm^{-3})	N_A (cm^{-3})	$E_A - E_V$ (meV)	N_D (cm^{-3})	$E_D - E_V$ (meV)
318.2	$1.83 \times 10^{18} \left[\dfrac{T}{300}\right]^{3/2}$	$7.31 \times 10^{17} \left[\dfrac{T}{300}\right]^{3/2}$	1.67×10^{18}	167.7	2.22×10^{17}	141.9
μ_p^0 (cm^2/V s)	α_p	$A_p(k/e)$ unit	μ_n^0 (cm^2/V s)	α_n	$A_n(k/e)$ unit	
27.99	-1.3 (-1.5)	4 (2)	5.42	-2 (-1.5)	3 (2)	

tions of the two bands and is given by[9]

$$S = \frac{\sigma_n S_n + \sigma_p S_p}{\sigma}$$

with

$$S_n = -\frac{k}{e}\left[\frac{E_c - E_F}{kT} + A_n\right]$$

and

$$S_p = \frac{k}{e}\left[\frac{E_F - E_V}{kT} + A_p\right].$$

The kinetic terms A_n and A_p depend on the scattering mechanisms

$$A_n = \tfrac{7}{2} + \alpha_n \quad \text{and} \quad A_p = \tfrac{7}{2} + \alpha_p.$$

Hall coefficient R_H obeys the law

$$R_H = \frac{1}{e}\frac{p\langle\mu_p^2\rangle - n\langle\mu_n^2\rangle}{(p\langle\mu_p\rangle + n\langle\mu_n\rangle)^2},$$

where $\langle\ \rangle$ is the mean value, and for this type of scattering $\langle\mu^2\rangle = r\langle\mu\rangle^2 = (3\pi/8)\langle\mu\rangle^2$.

The theoretical values of the physical constants deduced from all the experimental results are given in Table II. The equivalent density of states in the valence band and the conduction band as well as the deep-level concentrations N_A and N_D are specified. The carrier's mobilities and the exponents are also given. The theoretical curves for $\log_{10}$, S, and $\log_{10}|R_H|$ versus $10^3/T$ are shown as solid lines in Figs. 2—4. There is good agreement between the experimental and theoretical curves.

The deep levels E_A and E_D are located close to the middle of the energy gap ($E_i - E_v$ is found equal to 0.16 eV). The acceptor-level number of states is greater than that of the donor level. The latter is closer to the valence band ($E_D - E_i = -17$ meV), while the acceptor level is closer to the conduction band ($E_A - E_i = 9$ meV). These levels are assumed to be concentrated at the single-energy values E_D and E_A, respectively. Their nature is that of classical impurity levels, but, as they are relatively far from the conduction and valence bands, they behave as steps for electronic transitions and pin the Fermi level E_F. However, a weak shifting of E_F occurs which explains the Hall-coefficient variations. The Fermi-level T dependence is shown in Fig. 5. The p character increases in the

intermediate temperature range and the Hall coefficient becomes positive.

The exponents α_n and α_p are equal to -2 and -1.3, respectively, to be compared to the theoretical value -1.5. The high α_n value may be explained by intervalleys transitions and/or by a weak extra scattering by optical modes. The carrier mobility values are not high in comparison with the silicium values

$$\mu_n^0 \simeq 28 \text{ cm}^2/\text{V s}$$

and

$$\mu_p^0 \simeq 5.4 \text{ cm}^2/\text{V s}$$

with

$$T_0 = 300 \text{ K}.$$

The kinetic terms A_n and A_p are equal to 3 and 4, respectively, to be compared to the theoretical value 2. However, under the assumption of a weak decrease of the energy gap,[10] according to $\Delta = \Delta_0 - \gamma T$, good agreement of A_n and A_p with the theoretical values should be obtained. With the equivalent density of states in the valence and the conduction bands being known, the hole and electron effective masses are estimated,

$$m_p^* = 0.17 \quad \text{and} \quad m_n^* = 0.09.$$

An idealized projection of the structure along $[0\bar{1}0]$ is shown in Fig. 6, which has been obtained from the $Sb_4Mo_{20}O_{62}$ lattice parameters given by Parmentier et al.[3] The Mo—O bond lengths of MoO_5 pyramids and the main angles O—Mo—O and O—Sb—O are given. The distorted octahedrons MoO_6 can be considered as distorted-square basis pyramids ($\sim C_{2v}$ point-group symmetry) with short axial bonds along the b axis which involves strong π bonding. The MoO_5 pyramids lie alternately along $[0\bar{1}0]$ and $[010]$ in the perovskite sequence $(Mo_1 - Mo_2 - Mo_3 - Mo_4)$ as well as in the hexagonal tungsten bronz (HTB) sequence $(Mo_5 - Mo_6)$. The short- and long-bond succession is due to a ferroelectric distortion related to the Mo shifting within the octahedrons. Thus narrow bonding and antibonding π bands are expected rather than those that are broad. Effectively, the covalent bonding Sb—O where O is an oxygen atom of the framework MoO_6 compete with the π bonding Mo—O, and the e_g and t_{2g} orbitals lead to A_1, A_2 and $A_1(x,y)$, $B_1(xz), B_2(yz)$ orbitals, respectively, in C_{2v} symmetry.
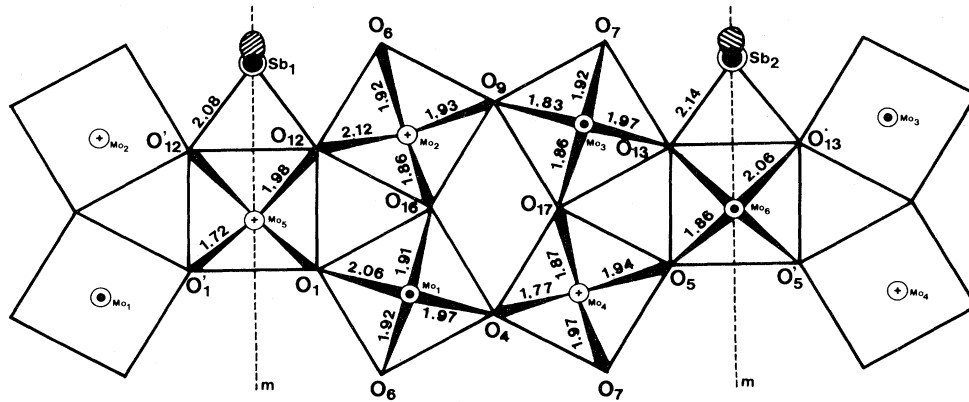
FIG. 6. Idealized projection of the $Sb_4Mo_{20}O_{62}$ structure along $\{010\}$.

These narrow π bands must be more or less stabilized according to the orbital nature.

In Fig. 6 the b axis is chosen as the z axis and the x and y axes are chosen along $Mo_5O'_1$ and Mo_5O_1, respectively. Deep π levels may be formed from d_{xz}, d_{yz} orbitals of all the Mo atoms, while d_{xy} orbitals of some Mo atoms such as Mo_3 (1.83-Å bonding), Mo_4 (1.77 Å), Mo_5 (1.72 Å) may lead to narrow bonding π bands lying above and forming the top of the valence band. The bottom of the conduction band may be formed from the empty antibonding π^* band rather than from the antibonding σ^* band which must be located higher in the energy range.

Some Mo atoms, such as Mo_1 and Mo_2, must not take part in the π bonding according to the Mo—O bonding lengths. The donor level may be formed from the nonbonding d_{xy} orbital of the Mo_1 atom, the neighborhood of which is more regular. Consequently, the acceptor level may be issued from the $Mo_2 d_{xy}$ orbital.

The schematic band model we propose for the $Sb_4Mo_{20}O_{62}$ compound is shown in Fig. 7. These assumptions are based on the room-temperature $Sb_4Mo_{20}O_{62}$ structure (spatial group $Pma2$). At lower temperatures,

more significant distortions are likely to appear which would permit one to find the origin of the E_A and E_D levels. However, a single line which confirms the presence of M_0^V is observed by EPR measurements.[11] The T dependence of its width (ΔH_{pp}) is shown in Fig. 8. The line width remains constant up to 140 K. This shows that the $4d^1$ electron is trapped on a single site. Therefore, the assumption that the donor level is an energy band must be excluded. At higher temperatures, the increase of the EPR line width shows the delocalization of this electron which is allowed to effect transitions between the acceptor and donor levels. The activation energy deduced from the $\log_{10}\Delta H_{pp}$ variations with the reciprocal temperature $[\Delta H = K\exp - \beta(\Delta E/2)]$, is about 26 meV. However, this energy must not be necessarily equal to that of the pseudogap transition ($E_A - E_D \simeq 25$ meV) because only local moments are tested by EPR measurements. The spin density calculated at 140 K by $CuSO_4 \cdot 5H_2O$ standard reference is about 10^{18} cm^{-3} to be compared to the value which can be deduced from transport measurements $(0.8 \times 10^{17}$ cm$^{-3})$ at the same temperature.

IV. CONCLUSION

The p-type semiconducting behavior of compact $Sb_4Mo_{20}O_{62}$ polycrystalline compounds has been shown. The schematic band structure which is deduced from transport measurements is in good agreement with later
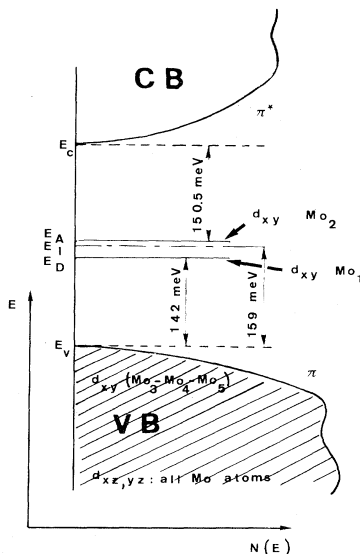
FIG. 7. $Sb_4Mo_{20}O_{62}$ schematic band model.
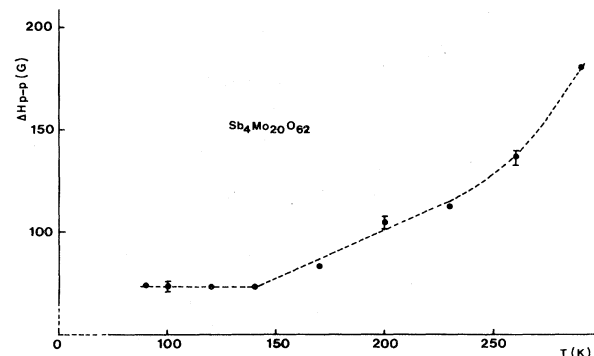
FIG. 8. Experimental variations of $\log_{10}\Delta H_{pp}$ versus $10^3/T$.

EPR experimental measurement results. The high TEP value at low temperatures and the Hall-coefficient variations cannot be explained by a simpler model with a single widened level. Otherwise, an extra contribution to the transport properties, due to a hopping conduction mechanism in the widened acceptor and donor levels, has been tested, but the best results are obtained without this extra contribution.

A model with two scattering mechanisms, i.e., ionized impurities and acoustical phonons, has also been tested: it has been found that the lattice scattering is the mostly predominant mechanism in the temperature range investigated. For the theoretical fitting, the activation energy which has been found is that which can be directly deduced from the experimental conductivity curve. The Hall coefficient and electrical conductivity have been used to scale the carrier's concentrations and mobilities, respectively, otherwise the mobility exponents and TEP kinetic terms were not allowed to depart much from the theoretical values of the different tested scattering mechanisms. Therefore, only four parameters, i.e., the mobility ratio and the three concentration ratios, have been used in order to fit all the experimental results.

In spite of some departures between samples being issued from different preparations, the concentrations, mobilities, and the nature of the scattering mechanisms of the carriers have been deduced from transport measurements. The good agreement between experimental (including EPR measurements) and theoretical results over a wide temperature range, without using any asymptotic behavior for the calculation of the carriers densities, confirms the validity of the model which has been retained.

[1]H. B. Goodenough, in Oxydes des Métaux de Transition, edited by G. Villars (unpublished).

[2]L. D. Ellerbec, H. R. Shanks, P. H. Sidles, and G. Danielson, J. Chem. Phys. 38, 298 (1961); H. R. Shanks, P. H. Sidles, and G. Danielson, Adv. Chem. 30, 237 (1963); R. K. Stanley, R. C. Morris, and W. G. Moulton, Phys. Rev. B 20, 5 (1979); 20, 1903 (1979).

[3]M. Parmentier, C. Gleitzer, and R. J. D. Tilley, J. Solid State Chem. 31, 305 (1980).

[4]A. Bonnet, P. Said, and A. Conan, Rev. Phys. Appl. 17, 701 (1982).

[5]D. Ramoul, A. Conan, Rev. Phys. Appl. 17, 145 (1982).

[6]A. Vapaille, Physique des Dispositifs à Semiconducteurs (unpublished).

[7]J. M. Ziman, Electrons and Phonons, (Clarendon, Oxford, 1967).

[8]Solid State Theory, edited by P. T. Landsberg, (Wiley-Interscience, New York, 1969).

[9]D. K. C. MacDonald, Thermoelectricity (Wiley, New York, 1962).

[10]D. Emin, Solid State Commun. 22, 409 (1977).

[11]M. Ganne and W. Glaunsiger (unpublished).